



# The effects of vortex breakdown bubbles on the mixing environment inside a base driven bioreactor

Stuart J. Cogan <sup>\*</sup>, Kris Ryan, Gregory J. Sheard

*Fluids Laboratory for Aeronautical and Industrial Research (FLAIR), Department of Mechanical and Aerospace Engineering, Monash University, Melbourne 3800, Australia*

## ARTICLE INFO

### Article history:

Received 7 September 2010  
Received in revised form 16 September 2010  
Accepted 16 September 2010  
Available online 20 October 2010

### Keywords:

Bioreactor  
Tissue engineering  
Vortex breakdown  
Mixing

## ABSTRACT

The bubble-type vortex breakdown inside a cylinder with flow driven by rotation of the base, has applications in mixing. We investigate this phenomena and its effect on the environment inside an open cylinder, with potential application as a tissue-engineering bioreactor, with tissue-scaffolds of two different geometries immersed in the fluid. Addition of scaffolds induces a blockage effect, hindering the flow in the central vortex core returning to the rotating base. This promotes early onset of vortex breakdown and alters the final shape of vortex breakdown bubbles. Placement of the scaffolds centrally on the cylinder axis yields almost identical levels and distributions of shear stress between the upper and lower surfaces of scaffolds. A change from a disk shaped to an ellipsoidal scaffold, of the same size, reduces the intensity of the maximum shear stresses at the scaffold surface by up to 50%. There is a range of Reynolds numbers where increasing Reynolds number, and hence possibly increasing mixing efficiency, leads to a decrease in the maximum levels of fluid forces at the scaffold surfaces. This is an important conclusion for scaffold based tissue engineering where improved mixing is sought, but often sacrificed in favor of minimizing fluid forces.

Crown Copyright © 2010 Published by Elsevier Inc. All rights reserved.

## 1. Introduction

A bioreactor can be described as any vessel that combines cells, tissue or other organic matter, together with chemicals and nutrients, commonly known as culture medium, in a way such as to stimulate the reproduction and proliferation of said organic matter [1]. Generally they can be split into two classes, suspension based and scaffold based, where the organic matter being cultured is either suspended in the medium and harvested as a batch of cells and cell aggregates, or anchored to the surface and interior of a porous scaffold (either fixed in space or suspended in the fluid medium) and harvested as a single construct, respectively. This investigation will deal only with scaffold based tissue culture applications.

Over the past two decades numerous prototype bioreactors have been suggested for the production of cartilage, bone and other tissue types. A summary of various bioreactor types and their applications is given by Martin et al. [2]. Briefly, they include: simple petri-dish reactors which provide a static culture environment [3], mixed flasks which provide a well mixed turbulent environment [3], horizontal-axis rotating drum type reactors that provide a laminar mixing environment [4], and perfusion reactors where culture medium is actively perfused directly through the scaffold via pressure differential [5]. These configurations are the most common types that have been investigated and the results from numerous physical tests of these reactors with real tissue samples have shown that further design improvements are required before functional

<sup>\*</sup> Corresponding author. Tel.: +61 407 522 198.

E-mail addresses: [stuart.cogan@monash.edu](mailto:stuart.cogan@monash.edu) (S.J. Cogan), [kris.ryan@monash.edu](mailto:kris.ryan@monash.edu) (K. Ryan), [greg.sheard@monash.edu](mailto:greg.sheard@monash.edu) (G.J. Sheard).

tissue equivalents can be created *in vitro* [6]. The most common deficiencies amongst these reactors are: 1) lack of a spatially homogenous flow field in the vicinity of the scaffold construct causing non-uniform levels of nutrient absorption and physical force exposure over the surface area; 2) levels of physical forces that are inappropriate (non-physical) to the tissue being grown, this usually manifests as an undesirably high level of shear stress, but can also be insufficient levels of shear, as well as too much or too little compressive force; 3) insufficient mass transport through the flow field brought about by poor mixing mechanisms; and 4) the presence of turbulent structures in the flow which are non-physiological and can be seminal to the first three issues above.

Recently a concentric cylinder bioreactor for cartilage tissue engineering has been tested [7] and the results indicate that, for cartilage tissue at least, a hydrodynamic environment that provides a relatively uniform velocity field, uniform transport of matter to and from scaffold-construct surfaces, and uniform low level fluid induced forces, is ideal.

It is with the above ideas in mind that we proceed with the investigation of the flow environment inside a novel bioreactor design for scaffold based tissue culture. We investigate the flow inside an open circular cylinder, driven by the constant rotation of the cylinder base, beginning with the analysis of the flow patterns and the development of vortex breakdown bubbles (VBBs), in the absence of immersed bodies, before considering the effect of two different shaped bodies located in the flow on the cylinder axis, in the vicinity of the bubbles. Besides the well defined boundary conditions and presence of the free surface to facilitate oxygen exchange, it is the development of these VBBs that makes this apparatus unique among possible candidates for bioreactors. It has been postulated [8] that the slowly recirculating fluid inside the VBB may provide an improved, low shear, homogenous and highly controllable environment for scaffold culture. Numerous other advantages include the isolation of the fluid within the VBB with respect to the bulk flow [9], possibly allowing for direct injection of fresh nutrients and/or extraction of waste products, to and from the growing construct, respectively; as well as the multitude of sizes, shapes and interior flow velocities observed for VBB at different Reynolds numbers (see Brøns et al. [10], Iwatsu [11] for example). Here we conduct a more general investigation into the interaction between the construct and the bubble, and the effect of both bubble presence and construct shape on the forces seen by the construct surface, for a construct located in a fixed position in the vicinity of, but outside, the VBB.

## 2. Model description

### 2.1. Physical model and parameters

The physical system being investigated is shown schematically in Fig. 1, along with the base mesh used for the simulations in the cases with no immersed body present. The system consists of a circular cylinder of height  $H$  and radius  $R$ , with the height-to-radius ratio  $\Gamma = H/R$  fixed at  $\Gamma = 1.5$ . The top of the cylinder is open exposing the surface of the fluid of kinematic viscosity  $\nu$  to the atmosphere and allowing for the insertion and suspension of an object representing a scaffold construct. Typically these constructs are supported by thin needles of negligible diameter that have been shown to not significantly affect the flow when stationary and located on the cylinder axis [12]. Thus, we neglect the presence of these supporting needles.

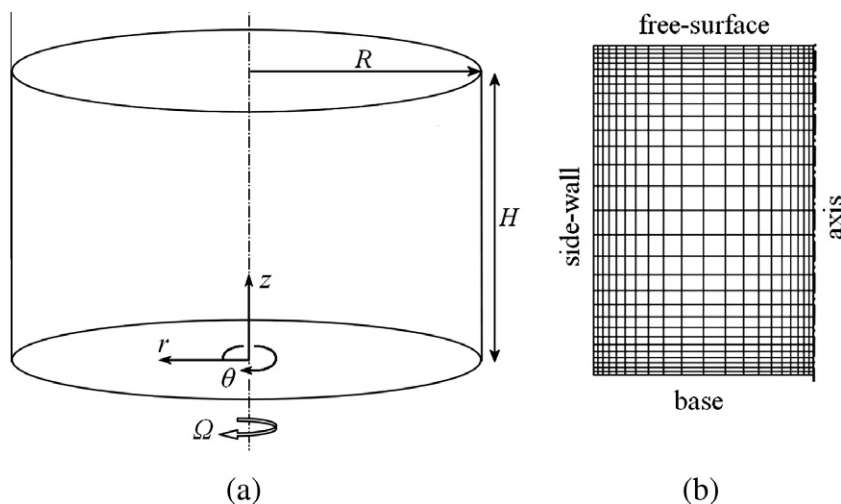


**Fig. 1.** Schematic diagram of geometry with no immersed body: (a) the bioreactor cylinder showing defining parameters and coordinate system, and (b) the base mesh showing spectral elements with boundary conditions labeled. The mesh represents an  $r$ - $z$  plane, one half (in this case the left half) of the meridional plane of the cylinder.

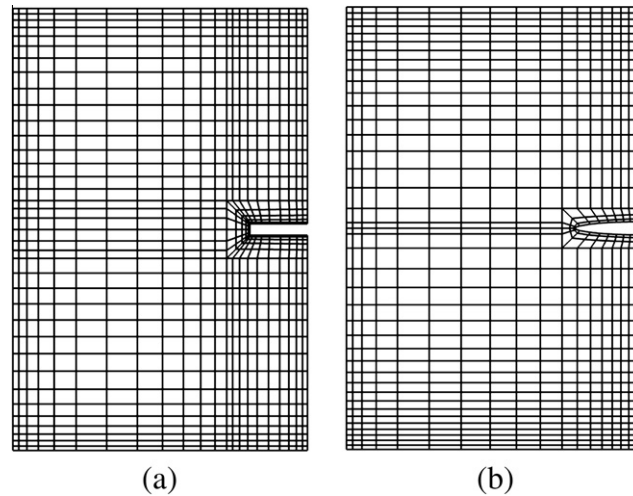


**Fig. 2.** Base meshes showing spectral elements for (a) the disk scaffold geometry, and (b) the ellipsoid geometry. In each case the right hand boundary is the cylinder axis for the axisymmetric systems.

The free surface is modeled as flat and stress-free throughout our investigation, an accurate assumption for cylinders with  $\Gamma > 1$  at Reynolds numbers in the range considered here [13]. The base rotates at a constant angular velocity  $\Omega$ , driving the flow and facilitating the mixing.

The scaffold profile under investigation takes one of two forms being either an axisymmetric disk or an ellipsoid (also axisymmetric), with axial dimension  $a$  and radial dimension  $b$ . In each case the centre of the scaffold is located midway up the cylinder axis. Scaffold dimensions were determined such that the ratio of vessel volume to scaffold volume was 1000:1 and the ratio of scaffold radius  $a$  to scaffold half height  $b$  was 10:1. These properties were chosen to be representative of common values from the tissue engineering literature (for example, Dusting et al. [8], Sucosky et al. [14], Vunjak-Novakovic et al. [15]). The base meshes employed for both construct geometries are shown in Fig. 2.

The Reynolds number for the system is defined as

$$Re = \frac{R^2 \Omega}{\nu} \quad (1)$$

and, together with the aspect ratio  $\Gamma$ , fully defines the ultimate flow-state of the system, for a given scaffold geometry. We consider a range of  $600 \leq Re \leq 2100$ . This represents a range of Reynolds numbers corresponding to common conditions, and characteristic Reynolds numbers encountered in the bioreactor literature [8,16]. We truncate our analysis at  $Re = 2100$  due to our desire to model the flow as axisymmetric. It has been shown previously that for enclosed cylinders (comprising a fixed-lid rather than free surface) axisymmetric flow conditions prevail up to at least the upper limit of our  $Re$  range and slightly beyond [17]. However, early indications from a linear stability analysis (not reported on here) are that the assumption of axisymmetry in the velocity field for *open* cylinders with  $\Gamma = 1.5$  loses validity beyond this Reynolds number.

A Froude number for the system may also be defined by

$$Fr = \frac{R\Omega}{g\Gamma}, \quad (2)$$

where  $g = 9.81 \text{ m/s}^2$  is the gravitational constant. Froude number can be used as a measure of the accuracy of the assumption that the top surface remains flat and hence the accuracy of our boundary condition. The magnitude of a vertical displacement of the free surface  $h$  obeys  $h/H \sim Fr$  [10,18,19]. For all simulation cases reported here Froude numbers were negligible, with the largest Froude number (re-scaled to typical laboratory conditions using a cylinder of radius  $R = 5 \text{ cm}$  and water as the working fluid) being of  $O(10^{-3})$ .

## 2.2. Governing equations and numerical treatment

In this study, lengths are normalised by the cylinder radius  $R$ , velocities by the product of the radius and the base angular velocity  $R\Omega$  and time by  $1/\Omega$ . The fluid in the cylinder is assumed incompressible and Newtonian throughout, thus conservation of momentum and mass for the fluid yield the Navier–Stokes equations, written here in vector form

$$\frac{\partial \mathbf{u}}{\partial t} + (\mathbf{u} \cdot \nabla) \mathbf{u} = -\nabla P + \nu \nabla^2 \mathbf{u}, \quad (3)$$

and the fluid continuity equation in vector form

$$\nabla \cdot \mathbf{u} = 0, \quad (4)$$

respectively, where  $\mathbf{u} = (u_z, u_r, u_\theta)(z, r, \theta)$  represents the vector velocity field in the cylindrical coordinate system,  $t$  is time and  $P = p/\rho$  is the kinematic scalar pressure field where  $p$  is the scalar pressure field and  $\rho$  is density.

Simulations are performed using an in-house package that utilises a nodal spectral element method to discretise the flow field in the meridional  $(r, z)$  semi-plane. The implementation of the spectral element method for spatial discretisation has been well documented, for example [20–22]. Within each spectral element flow variables are computed at Gauss–Legendre–Lobatto (GLL) quadrature points. The combination of high order polynomial shape functions used to compute flow variables over the GLL quadrature points on a sparse mesh and the governing equations being solved in weak form, following application of the Galerkin method of weighted residuals, allows for accurate simulations achieving spectral convergence. This approach has been successfully employed recently by Sheard and Ryan [23] and Sheard [24] and the algorithm has been validated against an independent spectral-element code [25]. Eqs. (2) and (3) are integrated forward in time using an operator-splitting technique and a third-order accurate backwards-multistep scheme. A full description of the method can be found in Karniadakis et al. [26].

The boundary conditions employed for the empty cylinder cases are: no-slip at the vertical sidewalls

$$(u_z, u_r, u_\theta) = 0 \quad \forall r = R, \quad (5)$$

a steady single component velocity along the base

$$(u_z, u_r, u_\theta) = (0, 0, r\Omega) \quad \forall z = 0 \cap r \neq R, \quad (6)$$

and a flat stress-free constraint on the surface, achieved via a symmetry condition

$$\left( u_z, \frac{\partial u_r}{\partial z}, \frac{\partial u_\theta}{\partial z} \right) = 0 \quad \forall z = H. \quad (7)$$

As the flow is known to be axisymmetric over the range of Reynolds numbers considered, only one half of the meridional plane is modeled, with a symmetry condition at the axis and all azimuthal derivatives set to zero throughout the domain. The boundary conditions remain the same when an immersed body is present on the axis, with the addition of a no-slip condition applied to the boundary representing the construct surface. The initial condition for the flow field is zero velocity throughout the domain and the base is set impulsively into motion. For all simulations a non dimensional time step of  $dt = 0.005$  was employed.

Final spatial resolution is determined at run time by specifying the order of interpolating polynomial within each spectral element. For all the results reported here, simulations were performed using polynomial interpolants of degree  $N_p = 9$ , over base grids containing 600, 882 and 748 spectral elements for the cases shown in Fig. 1(b), Fig. 2(a), and Fig. 2(b), respectively. These combinations were found to produce results accurate to 0.1% of very highly resolved reference cases. Fig. 3 shows the plot of percentage error against the degree of interpolating polynomial and demonstrates both the excellent convergence characteristics of the numerical package and the accuracy achieved using  $N_p = 9$ .

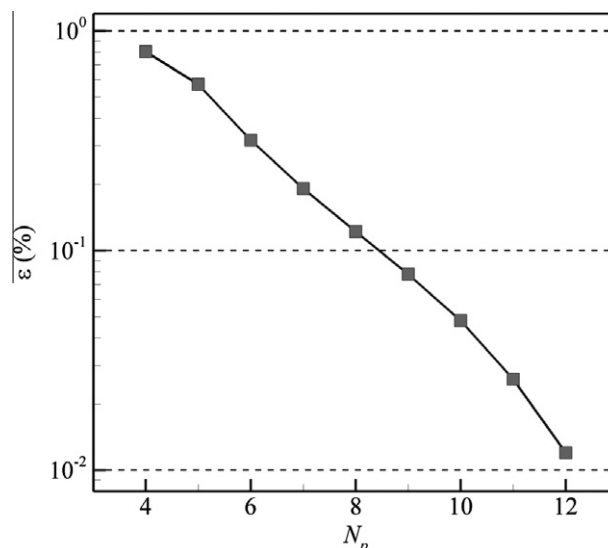
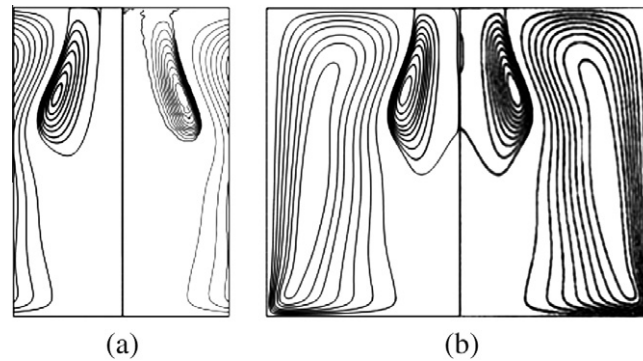


Fig. 3. The relative percentage error in the global  $L_2$  norm of the velocity field plotted with degree of interpolating polynomials.



**Fig. 4.** Comparisons of base flow streamlines with previously published data. In both images our own data is presented on the left hand side of the meridional plane as a mirror image of the original data on the right. Cases being compared are: (a)  $\Gamma = 1.45$  at  $Re = 2000$ , reprinted with permission from [27], copyright 2009, American Institute of Physics; and (b)  $\Gamma = 1.60$  at  $Re = 1980$ , reproduced with permission from [11]. In both cases good agreement was found.

We also validated our results for base flow streamline patterns against results from two prior investigations. The results are shown in Fig. 4 where, for each case, our own result is shown in the left half of the meridional plane and results of the other study are shown in the right half. The first is a recent experimental investigation [27] that used particle image velocimetry to analyse the flow in a cylinder of aspect ratio  $\Gamma = 1.45$ ; this comparison is made at  $Re = 2000$  and is shown in Fig. 4(a). Note that in this figure the extremities on either side are at  $r = R/2$ , as was the case in the original publication. The other is a numerical investigation that employed a different solver to that employed here [11]. This comparison was performed at  $\Gamma = 1.6$  and  $Re = 1980$ , and is shown in Fig. 4(b). Both comparisons show good agreement between our work and the previous study. A small corner bubble found at the axis inside the larger VBB by Iwatsu [11] and visible in the right half of Fig. 4(b) was identified in our investigation, however it was extremely slender and is only visible in the left half of Fig. 4(b) as a very slight deflection of the streamline at that location.

The final physical quantity that is of high importance to this study is the strain rate magnitude, an indicator of shear stress levels. The strain rate magnitude is defined as the leading eigenvalue of the strain rate tensor

$$S = \frac{1}{2}(V + V^T), \quad (8)$$

where  $V$  is a velocity-derivative tensor. In the cylindrical coordinate system employed by the solver it is defined as

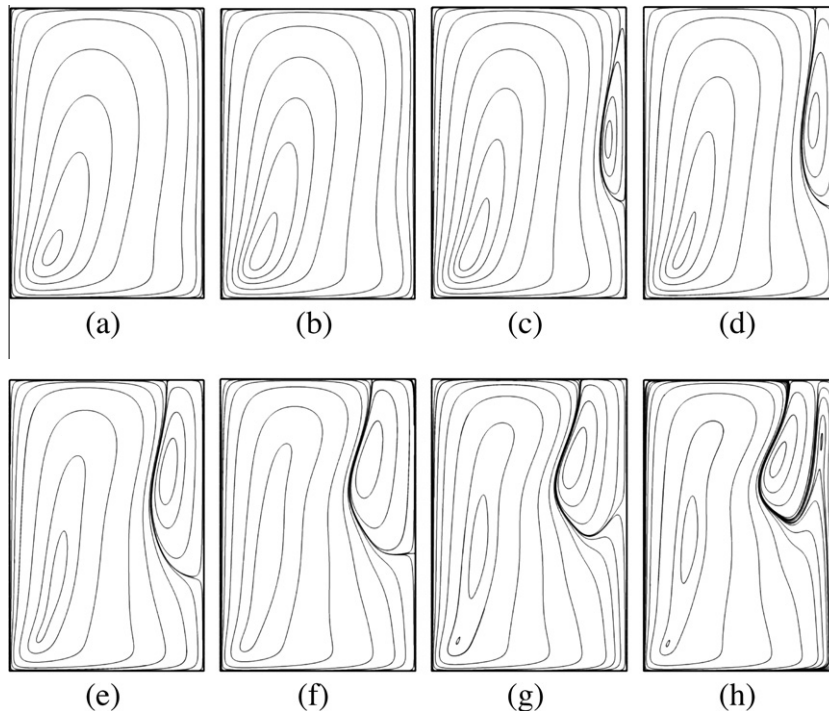
$$V = \begin{bmatrix} \frac{\partial u_z}{\partial z} & \frac{\partial u_z}{\partial r} & \frac{1}{r} \frac{\partial u_z}{\partial \theta} \\ \frac{\partial u_r}{\partial z} & \frac{\partial u_r}{\partial r} & \frac{1}{r} \left( \frac{\partial u_r}{\partial \theta} - u_\theta \right) \\ \frac{\partial u_\theta}{\partial z} & \frac{\partial u_\theta}{\partial r} & \frac{1}{r} \left( \frac{\partial u_\theta}{\partial \theta} + u_r \right) \end{bmatrix}. \quad (9)$$

### 3. Results

#### 3.1. Base flow without immersed body

For the empty vessel, rotation of the base at constant angular velocity  $\Omega$  drives the swirling flow by imparting angular momentum to the fluid adjacent to it. The fluid in the boundary layer that forms on the disk (known as an Ekman layer) is dragged by viscous stresses in the azimuthal direction [28], creating the primary swirling flow. The flow in the boundary layer also has a radial flow component which transports angular momentum towards the cylinder outer walls where it is turned in the positive axial direction. The fluid then flows up towards the surface until Froude number constraints at the surface force the fluid to return to the inner part of the cylinder where, upon colliding with the fluid returning from other parts of the perimeter, it is turned in the negative axial direction forming the much studied secondary over-turning meridional flow.

This basic state is shown in Fig. 5(a) for  $Re = 600$ , where the left hand side of the meridional plane is shown, such that the right hand edge of the figure represents the cylinder axis. As Reynolds number is increased, fluid with more and more angular momentum is forced to smaller radii by the overturning flow in the upper half of the cylinder, and the streamlines in the meridional plane are forced to gradually redistribute in such a way as to satisfy conservation of momentum. At some point near the axis a localised region of azimuthal vorticity develops, with opposite sign to that of the bulk flow, leading to an induced velocity in the positive axial direction. This induced velocity opposes the flow returning to the cylinder base down the central vortex core and a stagnation point forms on the axis where the magnitude of the negative axial velocity shrinks to zero. Thus the formation of the recirculation regions referred to as vortex breakdown bubbles.



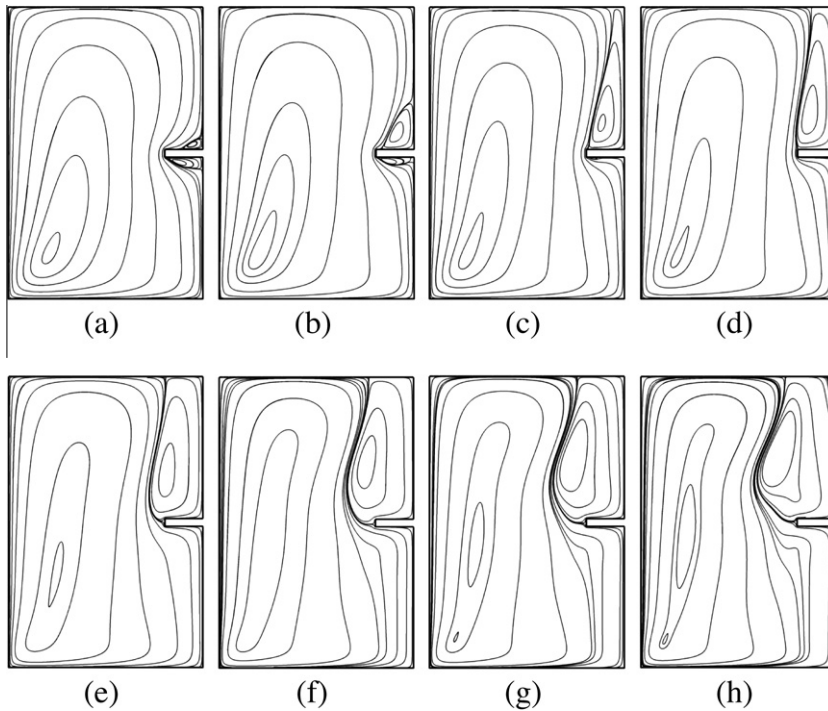
**Fig. 5.** Streamlines in the left meridional semi-plane detailing the evolution of the vortex breakdown flow with Reynolds number for the bioreactor without scaffold. Cases shown are: (a)  $Re = 600$ , (b)  $Re = 700$ , (c)  $Re = 800$ , (d)  $Re = 900$ , (e)  $Re = 1200$ , (f)  $Re = 1600$ , (g)  $Re = 1800$ , (h)  $Re = 2100$ .

Fig. 5 shows the evolution of the VBB as  $Re$  is increased. Initially appearing on the axis in the interior of the vessel, as  $Re$  is increased from 800 through to 1000 the bubble volume increases significantly as it expands both axially and radially. At a  $Re$  just less than 900 the bubble makes contact and merges with the free surface. This connection with the fluid-air interface is expected to provide a pathway for increased oxygen transport to the interior of the vessel, subject of a future investigation. As  $Re$  is further increased the VBB continues to expand radially around the mid-section, while beginning to contract axially from the lowest point. At  $Re \sim 1800$ , the streamlines around the left boundary of the VBB have become severely compressed, creating a shear layer of moderate strength between the bubble, with relatively slow moving fluid, and the primary cell of faster moving fluid. The bubble has reached its greatest radius by this stage and has begun to peel away from the axis at the downstream end. This process continues and is completed by  $Re \sim 2100$ , at which point the bubble has become completely removed from the cylinder axis and has formed a torus. This is the final state of the VBB flow in the axisymmetric regime.

### 3.2. Flow states in the presence of an immersed body

The sequence of frames in Fig. 6 shows flow states corresponding to the same  $Re$  that are shown in Fig. 5, but for the flow with a disk shaped scaffold-construct present at the axis. With the addition of a body on the cylinder axis there is an early onset of a quasi-vortex breakdown bubble state in the form of upstream and distal recirculation zones, adjacent to the upper and lower faces of the disk, respectively. These zones are already formed at our lowest  $Re = 600$  case, with the upper bubble initially only extending out to half the disk radius, from the axis, and the lower bubble appearing to envelop the whole underside of the disk. Increasing the  $Re$  to 700 sees this situation changed, the upstream bubble has expanded considerably both axially and radially and now extends the majority of the way out to the perimeter of the disk, a fivefold increase in size. At the same time the distal bubble has shrunk in size by around 25%, but still covers the majority of the underside of the disk. Neither of these states ( $Re = 600$  or  $Re = 700$ ) are likely conducive to tissue culture due to the non-uniform nature of flow over the construct surface, although the presence of recirculation zones would likely decrease the levels of shear at the scaffold surface due to lower fluid velocities.

By  $Re = 800$  the traditional VBB has developed upstream of the scaffold, with the last remnant of a distal bubble clinging to the underside of the tip. Upon further increase of  $Re$  the VBB once again begins to expand in the radial and axial directions and attach to the free surface, there is no longer any recirculation zone at the lower surface of the disk. By  $Re \sim 1000$  flow has begun to impinge almost normal to the tip of the scaffold (shown in Fig. 6(e) for  $Re = 1200$ ), this represents an interesting situation, with the direction of flow now uniform from the perimeter to the axis on both upper and lower surfaces of the disk. A flow state such as this could possibly be desirable from a tissue engineering perspective in that it may help to promote uniform growth on both surfaces. This situation continues for the remainder of  $Re$  considered, with the bubble volume



**Fig. 6.** Streamlines in the left meridional semi-plane detailing the evolution of the vortex breakdown flow with Reynolds number for the bioreactor with disk-shaped scaffold. Cases shown are: (a)  $Re = 600$ , (b)  $Re = 700$ , (c)  $Re = 800$ , (d)  $Re = 900$ , (e)  $Re = 1200$ , (f)  $Re = 1600$ , (g)  $Re = 1800$ , (h)  $Re = 2100$ .

also continuing to increase steadily as the radial expansion continues. The bubble is no longer able to separate from the axis due to the blockage effect of the presence of the disk, and this time the final state has a very large deformed bubble extending

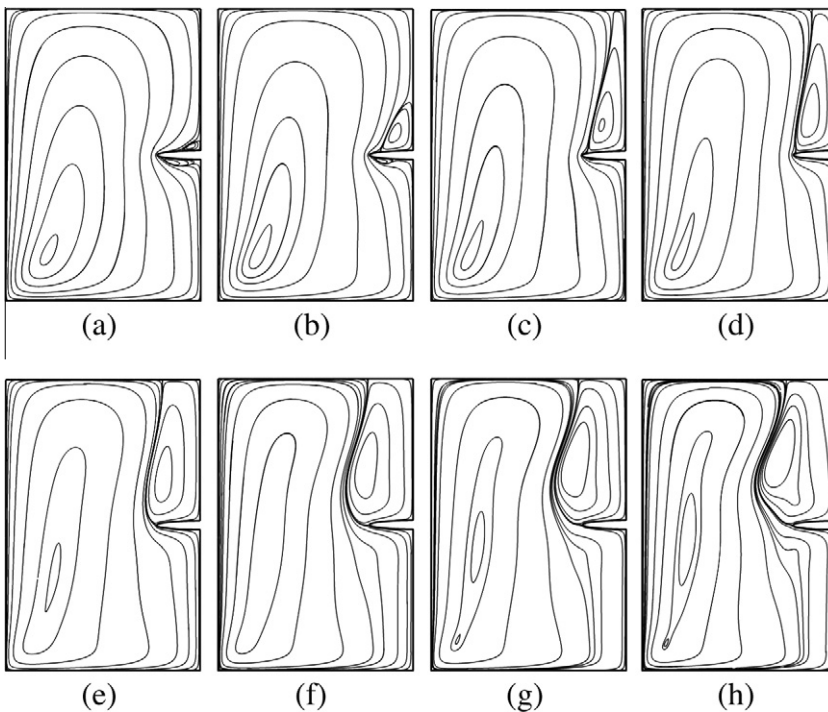


**Fig. 7.** Streamlines in the left meridional semi-plane detailing the evolution of the vortex breakdown flow with Reynolds number for the bioreactor with ellipsoid-shaped scaffold. Cases shown are: (a)  $Re = 600$ , (b)  $Re = 700$ , (c)  $Re = 800$ , (d)  $Re = 900$ , (e)  $Re = 1200$ , (f)  $Re = 1600$ , (g)  $Re = 1800$ , (h)  $Re = 2100$ .

from the free surface to the upper face of the scaffold, dominating almost 25% of the area of the meridional semi-plane, with a much smaller, tertiary circulation cell appearing on the cylinder axis, adjacent to the free surface.

For reliable assessment of the flow states at higher  $Re$  than those considered here, three dimensional computations are required. These will be the subject of future investigation, although it is likely that any major increase in  $Re$  above the present range would not be beneficial to growing many tissue types as most mammalian cells tend to respond poorly to the increased levels of fluid induced forces associated with increases in  $Re$ .

Modifying the shape of the scaffold to an elliptical profile, while keeping the same volume and length ratios described above, appeared to have little effect on the flow structures observed. Fig. 7 shows the evolution of the flow for the ellipsoid-scaffolds for the same range of  $Re$  as in Figs. 5 and 6. Over much of the range there was little discernable difference in the flow structures themselves between the two scaffold geometries. At  $Re = 600$  the upper bubble is basically identical to the disk-scaffold case, but the lower bubble is slightly smaller and is not attached to the axis. This bubble is a simple recirculation zone (in the backwards facing step sense) rather than a VBB. With an increase of  $Re$  to 700 the upper VBB increases in size similarly to the disk-scaffold case but the lower bubble has contracted significantly further. At both of these Reynolds numbers the flow conditions at the upper and lower surfaces of the disk scaffold look to be more uniform than those at the upper and lower surfaces of the ellipsoid scaffold. The range  $800 \leq Re \leq 1800$  reveals flow patterns almost identical between the two scaffold shapes, as evidenced (for example) by comparison of parts (c) through (f) in each of Figs. 6 and 7.

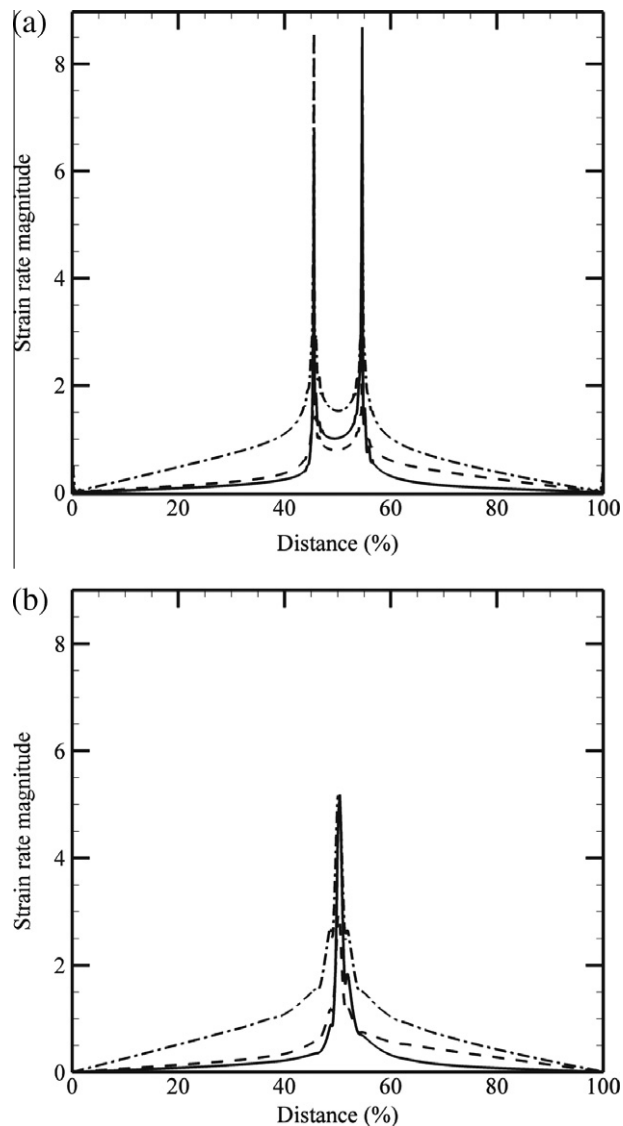


**Fig. 8.** Change in strain rate magnitude over (a) disk-scaffold surface, and (b) ellipsoid-scaffold surface. Distance is in percent of total perimeter distance, starting from the point on the axis at the downstream face of the scaffold, ending on the axis at the upstream face. Solid lines:  $Re = 600$ , dashed lines:  $Re = 1000$ , dash-dot lines:  $Re = 2100$ .

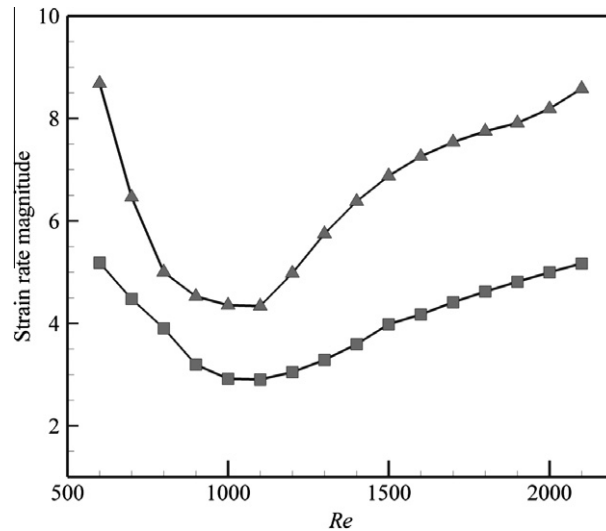


**Fig. 9.** Maximum values of the strain rate magnitude at scaffold construct surfaces plotted against Reynolds number. Triangles: disk-scaffold. Squares: ellipsoid-scaffold.

This trend continues until  $Re = 2100$  where we observe a flow field for the ellipsoid scaffold case almost identical to that of the disk-scaffold at the same  $Re$ , but with no tertiary corner bubble present. The absence of this tertiary bubble is unlikely to affect the flow field in the vicinity of the scaffold, although it may have some slight impact on nutrient transport within the bubble and on the placement of any automated nutrient-injection/waste-removal system. The mass transport of scalar quantities (such as oxygen for example) is the subject of ongoing work and will be included in a future article.

Fig. 8(a) and Fig. 8(b) allow for a more quantitative analysis of the different flow environments experienced by the two different scaffolds. They show the level of strain rate, a direct indicator of shear stress for axisymmetric flows of Newtonian fluids, at the scaffold surface as a function of position along the line tracing the scaffold perimeter, beginning at the downstream axial location and ending at the intersection of the axis and the upstream scaffold face. Three Reynolds numbers are shown for comparison,  $Re = 600, 1000$ , and  $2100$ . It is immediately observable that the sharp corners of the disk-scaffold lead to a significant increase in the maximum computed levels of strain and that two localised maxima exist corresponding to the disk scaffold edges. These are in contrast to the single smaller peak forming as a result of the curvature at the edge of the ellipsoid scaffold. In general, levels of strain along a given surface (upper or lower) are relatively uniform between the two scaffolds compared to maxima (for example, comparing the strain rate values in the distance-range zero to thirty-five percent for the solid lines on each plot), particularly at the lower Reynolds numbers. However, there is a slight non-uniformity about the strain rate profiles between the upper and lower surfaces for a given scaffold geometry at a given Reynolds number. The severity of this decreases as  $Re$  is increased, observable by comparing the left hand side with the right hand side for either of the  $Re = 2100$  curves, and then doing the same for the corresponding  $Re = 600$  curve. These observations are in-line with the predictions from the plots of flow structures that are less uniform between top and bottom surfaces of scaffold at lower  $Re$ . Also worth noting is the fact that the two maxima that exist in the disk-scaffold cases are not of equal magnitude. It was found that these can vary by up to 31%. This is an undesirable phenomenon when attempting to encourage uniform growth.

A pleasing result not directly observable in Fig. 8, due to the close proximity of the lines in those plots, is shown in Fig. 9. The maximum result of strain rate computed at the surface of each construct is plotted with  $Re$ . It shows that for a significant part of the  $Re$  range the maximum value of strain rate (and hence shear stress) experienced at a point on the construct surface actually decreases with increasing  $Re$ . This result is somewhat counter-intuitive as an increase in  $Re$  is usually associated with an increase in velocity throughout the flow field, for a given Newtonian fluid, and hence higher levels of shear stress at no slip surfaces. Certainly of import to the tissue engineering capabilities of a given bioreactor is maximising the mixing and nutrient transport potential while minimising exposure of tissue constructs to harmful levels of fluid forces. The ability to increase the  $Re$ , thereby possibly increasing the vessel's mixing capability, while at the same time reducing the maximum levels of shear stress acting on immersed bodies may be extremely beneficial. Fig. 9 indicates that the present vessel may provide such capabilities over at least the range  $600 \leq Re \leq 1100$ . Also reinforced by Fig. 9 is the large decrease in maximum strain between the disk and ellipsoid scaffold shapes, with a drop of up to 65% achievable over the whole  $Re$  range and drops of approximately 50% achievable for a given  $Re$ . If nothing else, this would advocate a move away from the disk shaped scaffolds, currently employed by the majority of physical researchers in the area of tissue engineering, in applications where the bio-matter is adversely affected by high levels of shear.

## 4. Conclusions

An investigation into the suitability of a simple base-driven cylinder flow for use in tissue engineering has been performed. Results revealed numerous different vortex breakdown flow states occurred depending primarily on Reynolds number (mixing intensity) and the existence or absence of objects located centrally on the cylinder axis. To a lesser extent the flow states were also affected by the geometry of the tissue-scaffold-construct being used: a common disk-shaped scaffold with sharp edges, contrasted with an ellipsoidal-shaped scaffold of same size but with smooth edges. These flow states observed have been presented and analysed for the distribution of strain rate (an indicator of fluid shear stress levels) over the scaffold surfaces. It was found that the strain rate distributions were relatively uniform between the top and bottom surfaces of scaffolds, for a given scaffold type, and that increasing Reynolds number improved the uniformity. This is likely due to the change in structure of the vortex breakdown bubbles, from allowing the axial flow to impinge onto the scaffold upper surface at lower Reynolds numbers, to the flow impinging approximately orthogonally to the outer edge of the scaffold as Reynolds number increased. However this improvement in uniformity of strain rate distribution came at the expense of an increased strain rate magnitude over the entire scaffold surface. A comparison of the maximum recorded levels of strain rate between the two scaffold geometries over a range of Reynolds numbers has also been presented. The ellipsoid geometry was subject to significantly lower levels of maximum strain rate and hence shear stresses across the entire range of  $Re$ . Finally, it is suggested that a range of interim Reynolds numbers,  $600 \leq Re \leq 1100$ , may provide an optimal regime for tissue culture in these vessels. This was based on the requirement to maximise mass transport and mixing while keeping fluid induced forces to a minimum. Fully 3D simulations at slightly higher  $Re$  may reveal further benefits, and are the focus of ongoing investigation.

## Acknowledgements

This research was undertaken in part using the NCI National Facility in Canberra, Australia, thanks to a Merit Allocation Scheme grant. NCI is supported by the Australian Commonwealth Government. The authors thank the Monash University Faculty of Engineering for financial support in the form of Engineering small grants. S.J.C thanks the Department of Mechanical and Aerospace Engineering at Monash University for ongoing financial support in the form of a Monash Departmental Scholarship, and the Monash eResearch Centre for access to their High Performance Computing facility.

## References

- [1] E. Darling, K. Athanasiou, Articular Cartilage Bioreactors and Bioprocesses, *Tissue Eng.* 9 (2003) 9–26.
- [2] I. Martin, D. Wendt, M. Heberer, The role of bioreactors in tissue engineering, *Trends Biotechnol.* 22 (2004) 80–86.
- [3] G. Vunjak-Novakovic, L. Freed, R. Biron, R. Langer, Effects of mixing on the composition and morphology of tissue-engineered cartilage, *AIChE J.* 42 (1996) 850–860.
- [4] C. Begley, S. Kleis, The fluid dynamic and shear environment in the NASA/JSC rotating-wall perfused-vessel bioreactor, *Biotechnol. Bioeng.* 70 (2000) 32–40.
- [5] L. Niklason, J. Gao, W. Abbott, K. Hirschi, S. Houser, R. Marini, R. Langer, Functional arteries grown in vitro, *Science* 284 (1999) 489.
- [6] G. Vunjak-Novakovic, The fundamentals of tissue engineering: scaffolds and bioreactors, in: *Novartis Found Symp.*, John Wiley, Chichester, New York, 1999, pp. 34–45.
- [7] S. Saini, T. Wick, Concentric cylinder bioreactor for production of tissue engineered cartilage: effect of seeding density and hydrodynamic loading on construct development, *Biotechnol. Prog.* 19 (2003) 510–521.
- [8] J. Dusting, J. Sheridan, K. Hourigan, A fluid dynamics approach to bioreactor design for cell and tissue culture, *Biotechnol. Bioeng.* 94 (2006) 1196.
- [9] M. Thompson, K. Hourigan, The sensitivity of steady vortex breakdown bubbles in confined cylinder flows to rotating lid misalignment, *J. Fluid Mech.* 496 (2003) 129–138.
- [10] M. Brøns, L. Voigt, J. Sørensen, Topology of vortex breakdown bubbles in a cylinder with a rotating bottom and a free surface, *J. Fluid Mech.* 428 (2001) 133–148.
- [11] R. Iwatsu, Numerical study of flows in a cylindrical container with rotating bottom and top flat free surface, *J. Phys. Soc. Jpn.* 74 (2005) 333–344.
- [12] H. Husain, V. Shtern, F. Hussain, Control of vortex breakdown by addition of near-axis swirl, *Phys. Fluids* 15 (2003) 271–279.
- [13] J. Lopez, F. Marques, A. Hirta, R. Miraghaie, Symmetry breaking in free-surface cylinder flows, *J. Fluid Mech.* 502 (2004) 99–126.
- [14] P. Sucusky, D. Osorio, J. Brown, G. Neitzel, Fluid mechanics of a spinner-flask bioreactor, *Biotechnol. Bioeng.* 85 (2004) 34–46.
- [15] G. Vunjak-Novakovic, B. Obradovic, I. Martin, P. Bursac, R. Langer, L. Freed, Dynamic cell seeding of polymer scaffolds for cartilage tissue engineering, *Biotechnol. Prog.* 14 (1998) 193–202.
- [16] D. Wootton, D. Ku, Fluid mechanics of vascular systems, diseases, and thrombosis, *Ann. Rev. Biomed. Eng.* 1 (1999) 299–329.
- [17] A. Gelfgat, P. Bar-Yoseph, A. Solan, Three-dimensional instability of axisymmetric flow in a rotating lid-cylinder enclosure, *J. Fluid Mech.* 438 (2001) 363–377.
- [18] J. Lopez, Unsteady swirling flow in an enclosed cylinder with reflectional symmetry, *Phys. Fluids* 7 (1995) 2700–2714.
- [19] A. Spohn, M. Mory, E. Hopfinger, Observations of vortex breakdown in an open cylindrical container with a rotating bottom, *Exp. Fluids* 14 (1993) 70–77.
- [20] A. Patera, A spectral element method for fluid dynamics: laminar flow in a channel expansion, *J. Comput. Phys.* 54 (1984) 468–488.
- [21] A. Tomboulides, S. Orszag, Numerical investigation of transitional and weak turbulent flow past a sphere, *J. Fluid Mech.* 416 (2000) 45–73.
- [22] H. Blackburn, J. Lopez, Modulated rotating waves in an enclosed swirling flow, *J. Fluid Mech.* 465 (2002) 33–58.
- [23] G. Sheard, K. Ryan, Pressure-driven flow past spheres moving in a circular tube, *J. Fluid Mech.* 592 (2007) 233–262.
- [24] G. Sheard, Flow dynamics and wall shear-stress variation in a fusiform aneurysm, *J. Eng. Math.* 64 (2009) 379–390.
- [25] H.M. Blackburn, G.J. Sheard, On quasi-periodic and subharmonic Floquet wake instabilities, *Phys. Fluids* 22 (2010) 031701:1–031710:4.
- [26] G. Karniadakis, M. Israeli, S. Orszag, High-order splitting methods for the incompressible Navier–Stokes equations, *J. Comp. Phys.* 97 (1991) 414–443.
- [27] D. Lo Jacono, M. Nazzarini, M. Brøns, Experimental vortex breakdown topology in a cylinder with a free surface, *Phys. Fluids* 21 (2009) 111704.
- [28] J. Healey, Instabilities of flows due to rotating disks: preface, *J. Eng. Math.* 57 (2007) 199–204.